Hindawi
Shock and Vibration
Volume 2023, Article ID 3029133, 15 pages
https://doi.org/10.1155/2023/3029133

Research Article

Study on Construction Response Characteristics of Large Cross-Section Tunnel Crossing Huge Karst Cave Backfill

Yunteng Chen,[1] Yuancheng Cai ,[2] Jianwei Zhang,[2] Jie Li,[3] Xiaotong Huang,[4] Hao Lei,[5] and Peilong Yuan[2]

[1]*Shaoxing Communications Investment Group Co., Ltd., Shaoxing 312000, China*
[2]*School of Highway, Chang'an University, Xi'an 710064, China*
[3]*School of Energy and Architecture, Xi'an Aeronautical Institute, Xi'an 710077, China*
[4]*China Railway Construction Yunnan Investment Co., Ltd., Kunming 650216, China*
[5]*School of Civil Engineering, North Minzu University, Yin'chuan 750000, China*

Correspondence should be addressed to Yuancheng Cai; caiyuancheng@chd.edu.cn

Received 7 September 2022; Revised 25 February 2023; Accepted 7 April 2023; Published 22 May 2023

Academic Editor: Roberto Nascimbene

The existence of giant karst cave can cause collapse and water inrush hazards during the excavation of the karst tunnel, causing serious economic losses. In this paper, based on the FEA software MIDAS, a numerical simulation model for the backfilling of a large karst cave through a large cross-section tunnel was established. The distribution characteristics and change rules of the displacement field, stress field, horizontal support stress, and plastic zone of the tunnel surrounding rock and backfill were explored. The first stage of tunnel excavation leads to a sharp increase in the displacement of the tunnel's surrounding rock and the deterioration of the plastic zone, which should be strengthened and monitored. The tunnel arch, waist, and wall footing areas were prone to stress concentration. The two layers of horizontal support force show a certain regularity, showing a sharp increase and a gradually smooth growth trend. Meanwhile, the site monitoring results for arch settlement and horizontal convergence of the mega cavern tunnel were analyzed. The results show that the numerical calculation results were in good agreement with the values of site monitoring data. The average errors of final crown settlement and horizontal convergence were 8.6% and 15.9%, respectively, which verified the correctness of the numerical modeling method. This project can provide reliable experience for the construction of similar large cavern tunnels.

1. Introduction

In recent years, the number of tunnels built in karst landscapes has been increasing [1–6]. Due to the complexity and diversity of karst landscapes, a large number of water and mud inrush hazards and collapses have occurred during the construction of karst tunnels, causing huge losses of economic [7–18]. For example, the excavation face of the Chaoyang Tunnel encountered large karst caves, resulting in a water inrush disaster. A lining trolley was flushed out of the hole owing to the huge water pressure [19]. Another typical case was Lingjiao Tunnel, which was known as the largest mudslide disaster in Chinese history [20, 21]. More than 40000 m^3 of mud and a 12 m deep collapse pit were generated on the surface above the tunnel.

At present, a lot of research has been carried out on the construction response characteristics of karst tunnels [22–32]. Chen and Sha [33] studied the stability of the surrounding rock and the treatment structure during the Naqiu Tunnel excavation by means of field tests and numerical simulation. Li et al. [34] analyzed the influence of the size, volume, and location of karst caves on the displacement of different measuring points on the monitoring section through numerical simulation, and compared it with the situation without karst caves. Thus, a method for predicting the top of a hidden karst cave based on displacement monitoring during tunnel construction is proposed. Xu et al. [35] simplified the geological conceptual model through PANDAS software, established a numerical model, and discussed the influence of the location and size of the karst

cave and the distance between the tunnel and the karst cave on the principal stress and displacement of the surrounding rock. Zheng et al. [36] took the tunnel crossing, the largest karst cave in the history of China, as an example, and put forward a series of disposal schemes. The effectiveness of the scheme was verified by the field monitoring data, which laid a good foundation for the construction. Zhang et al. [37] established a three-dimensional numerical model to analyze the stress field and displacement field of surrounding rock after tunnel excavation around the karst cave, and revealed the variation law of the stress and displacement with tunnel excavation. Zhou et al. [38] used the three-dimensional finite element software ANSYS to simulate the interaction between the karst cave treatment structure and tunnel excavation of the Baishugong Tunnel, and evaluated the reinforcement effect of the support structure. Li et al. [39] explored the development law of the surrounding rock stress field and displacement field under the condition of changing the excavation size of the tunnel and the development size of the karst cave by using the self-developed large-scale model test system, and revealed the process of karst cave disaster.

The above studies show that most of the studies have focused on cavern solutions, and relatively few studies have been conducted on the construction response characteristics of huge cavern backfilling [40–51]. Although Chen et al. [52] studied the stress distribution and deformation of surrounding rock in their numerical simulation of a large karst cave in front of the Huaguoshan Tunnel. Li et al. [53] used the finite difference method to conduct three-dimensional simulation calculations on the existence of a karst cave and the stress distribution, displacement characteristics, and plastic zone size of surrounding rock before and after grouting filling and reinforcement. Lin [54] studied the mechanical response of surrounding rock in the process of crossing the giant karst cave in front of the full section and based on this, selected and optimized the structure. However, there are few studies on the construction response characteristics of a superlarge cross-section tunnel crossing a giant karst cave.

Therefore, based on the construction of the YJS tunnel crossing the huge karst cave backfill, the numerical simulation method was used to analyze the law in the horizontal convergence of each step. Meanwhile, the stress field distribution of the tunnel, the axial force of the transverse support, and the distribution characteristics of the plastic zone of the model were obtained. In view of the unstable stress and displacement of surrounding rock, a series of engineering countermeasures are proposed. The reliability of the numerical modeling method was further verified by site data. This study enriches the research status of a superlarge cross-section tunnel and a giant karst cave and has reference significance for the research and construction of similar projects.

2. Project Case

The tunnel is located between Xingwen and Weixin on the Cheng-gui Railway line in China [55]. The tunnel area is in the terrain of the transition from the Sichuan Basin to the Yunnan-Guizhou Plateau, with steep mountains, gullies, and valleys, large relative height differences, and strongly developed karst. The tunnel is 25.21 m high, 19.52 m wide, with a cross-sectional area of 432 m^2, a total tunnel length of 6306 m, and a maximum burial depth of 350 m. The top of the tunnel is located near the roof of the hall, and section D3K279 + 855~ + 960 crosses the cave hall. The direction of the line mileage and the main axis of the cave intersect at a large angle of 80°. The relationship between the tunnel and the cave is shown in Figure 1.

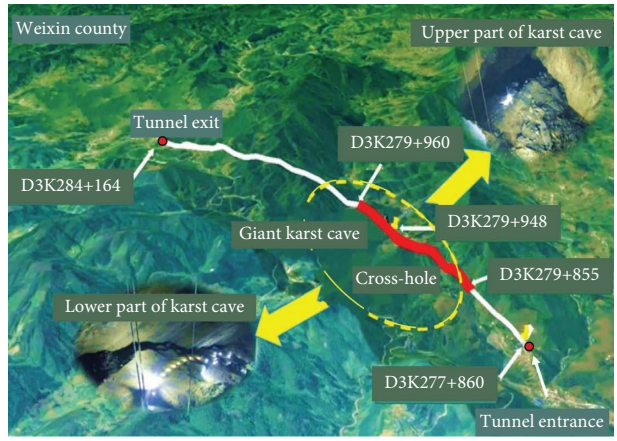

Figure 1: Tunnel location.

The cave is developed longitudinally for about 93 m along the line direction and laterally for about 230 m in the vertical line direction, roughly rectangular in shape [56, 57]. The top of the cave is dome-shaped, and the vertical height of the hall varies from 50 to 120 m. The bottom of the cave is filled with fill material, which is 30 to 90 m thick. The surface soil is yellow clay, under which is the cave fill material in the form of crushed stones, gravelly soil, medium-coarse sand, and fine pebbles. The cavern fill is dominated by crushed block stone soil, and according to the exploration, there are soft clay and other weak interlayers of 0–15 m thick distributed between them, with poor regularity. In addition, the accumulation is sloping from the top of the right side of the line to the bottom of the dark river, with a slope of 30–35°, and the rock body where the cavern is located is limestone. The construction plan is to excavate the backfill body after using slag and block backfill. A simplified geological cross-section is shown in Figure 2.

3. Numerical Simulation

3.1. Numerical Model. Midas/GTS is a finite element analysis software that organically combines the general finite element analysis kernel with the specialized requirements of geotechnical tunnel structures. Compared with other engineering software, the software has many advantages in use, such as fast and intuitive 3D modeling, professional geotechnical analysis functions, fast and accurate automatic mesh generation, and intuitive analysis results. The calculation and analysis results are relatively safe and favored by engineers. It has 15 kinds of intrinsic structure models and can customize the intrinsic structure models. The analysis

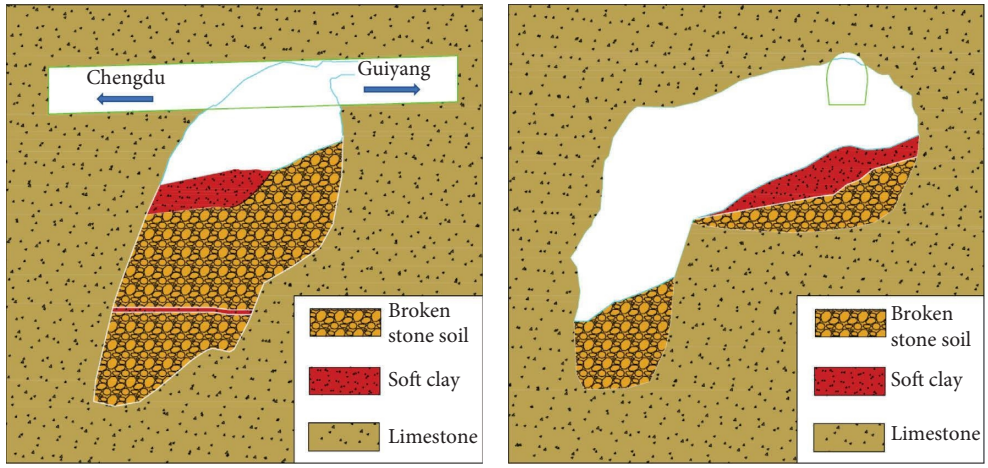

Figure 2: Location of the cavern in relation to the cross and longitudinal section of the tunnel. (a) Longitudinal section. (b) Cross-section.

functions available include construction phase analysis, static analysis, seepage analysis, dynamic analysis, and coupled seepage and stress analysis, covering almost all analysis functions in the tunneling field. The specific modeling process is shown in Figure 3.

The calculated dimensions of the model were $L \times W \times H = 300\,\text{m} \times 85\,\text{m} \times 300\,\text{m}$. The model range around the tunnel met 3–5 times the excavation section. The geometric boundary shape of the giant cavern is very complex, and it is simplified accordingly. The filling soil in the cavern is mainly broken stone soil and soft clay, and the upper part of the cavern is backfilled with rubble and spoil. The calculation model is shown in Figure 4.

The physical and mechanical parameters of the soil layers, backfill, support structure, reinforced soil layers, and the adopted intrinsic structure models are shown in Table 1. All materials are homogeneous, continuous, and isotropic. Limestone, crushed stone soil, soft clay, block stone, waste slag, the limestone, waste slag, and soft clay after reinforcement are simulated by a three-dimensional solid element, shotcrete is simulated by a slab element, and anchor rods and horizontal support are simulated by an embedded beam element.

The actual depth of the cavern is about 350 m. According to the self-weight stress $q = \gamma h = 27 \times 280 = 7560\,\text{kPa}$, a uniform load of 7560 kPa is applied to the upper part of the surrounding rock in the vertical direction of the model. In addition, the boundary conditions of the model are vertical restraint at the bottom and normal restraint around the perpendicular to the rock surface. The initial stress states are the self-weight stress and the upper vertical uniform load.

3.2. Construction Stages Simulation. The sixth bench excavation construction method was adopted. The whole construction process consists of six bench excavations and anchor shotcrete support as a cycle step. It mainly includes excavation, bolting and concreting support, lining construction, arch concrete backfilling, horizontal support construction, grouting reinforcement at both sides and bottom, horizontal support removal, and other construction stages. The construction process is shown in Table 2, and the important construction stages are shown in Figure 5.

The release of the accumulated elastic energy of the soil is simulated by setting the load release factor to avoid the unbalanced internal forces due to excavation being loaded onto the excavation stages at once. The excavation process is simulated by loading 40%, 30%, and 30% of the soil into different construction stages, gradually reducing the load by stages, and finally completely releasing the soil.

4. Result Analysis

4.1. Displacement Analysis

4.1.1. Arch Waist Displacement. As can be seen from Figure 6, the displacement of the surrounding rock on the left side of the tunnel axis shows a trend of settlement, while the right side shows a trend of uplift. This is due to the fact the tunnel is located on the upper right side of the giant karst cave, resulting in the surrounding rock on the left side being filled with waste slag, block stone, crushed stone soil, soft clay, and other backfill. Compared with the limestone on the right side, its strength is low, its vertical settlement is large, and the tunnel is in a biased state.

To further analyze its deformation law, a total of six measurement points at the arch waist on both sides of the three typical sections were selected for the study, and their displacement curves were made (Figures 7 and 8). It can be concluded that (1) the whole section of the first step of the tunnel is excavated, resulting in a rapid increase in the displacement value at the arch waist. The settlement of the left waist is 4.3 mm, and the uplift of the right side is 10.6 mm. However, if the bolt concrete support and grouting reinforcement measures are taken in time, the displacement can be well controlled. The growth rate of displacement on the left and right sides of the arch waist is significantly reduced. (2) The accumulated displacement at the arch waist

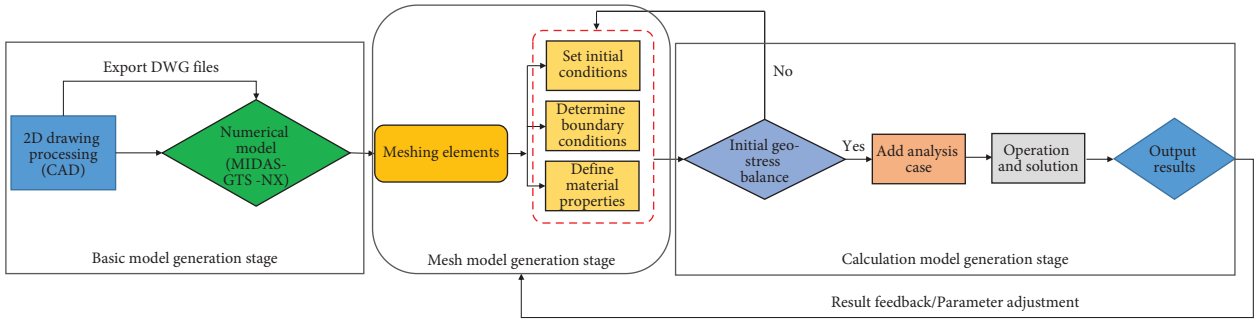

Figure 3: Modeling process.

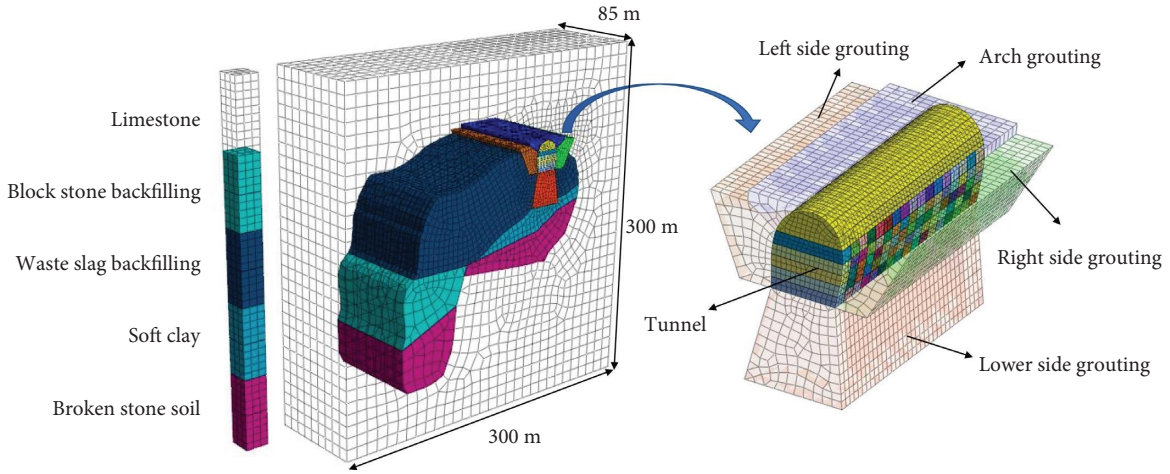

Figure 4: Numerical model.

Table 1: Material parameters.

Name	Model type	Elastic modulus (kPa)	Poisson's ratio	Bulk density (kN/m^3)	Cohesion (kN/m^2)	Internal friction angle (°)
Limestone	M-C	2.4×10^7	0.22	27	3000	40
Broken stone soil	M-C	1.0×10^5	0.3	20.5	5	31
Soft clay	M-C	5×10^3	0.4	19.5	24	10.3
Block stone	M-C	2.25×10^7	0.2	26.5	2900	38
Waste slag	M-C	2.25×10^7	0.2	26.5	2900	35
Horizontal support	Elastic	2.06×10^8	0.3	78.5	—	—
Shotcrete	Elastic	3×10^7	0.2	25	—	—
Bolt	Elastic	4.5×10^7	0.3	78.5	—	—
Limestone after reinforcement	Elastic	2.5×10^7	0.2	27	—	—
Waste slag after reinforcement	Elastic	3.4×10^7	0.2	26.5	—	—
Soft clay after reinforcement	Elastic	8.5×10^3	0.35	20	—	—

of the section at the measurement point is mainly caused by the excavation stage. Among them, about 92% of the total displacement at point 4 is caused by the excavation stage, and about 85% of the total displacement at points 5 and 6 is caused by the excavation stage. But with the application of horizontal support, the growth rate of displacement at waist gradually decreases, until the displacement value basically tends to stabilize and no longer grows after the application of grouting reinforcement to the backfill at the bottom of the tunnel. The relative displacement of the left and right sides of the waist was basically maintained at about 29 mm. It shows that the construction of horizontal supports and bottom grouting reinforcement are effective means to control the large rate of deformation of the arch waist during large section excavation in the backfill of a giant karst cave.

4.1.2. Horizontal Convergence. Figure 9 shows the construction steps-curve of cumulative horizontal convergence of section D3K279 + 916. It can be seen: (1) the horizontal convergence of the whole bench section increases rapidly in the excavation stage, and then it is in the slow growth stage

Table 2: Contents of the construction stage.

Construction stage	Concrete content
I.S.	Initial stress state, displacement clearing
S1	Excavation of 1st bench
S3	Arch concrete backfilling, grouting reinforcement, and support at both sides of the backfill body
S4	Excavation of 2nd bench
S5	Construction of 2nd bench support
S6	Excavation of 3rd bench
S7	Construct the 3rd bench support and arrange the horizontal support
S8	Excavation of 4th bench
S9	Construction of 4th bench support
S10	Excavation of 5th bench
S11	Construct the 5th bench support and arrange the horizontal support
S12	Excavation of 6th bench
S13	Construction of 6th bench support
S30	Grouting reinforcement of the bottom
S31	Remove the horizontal support

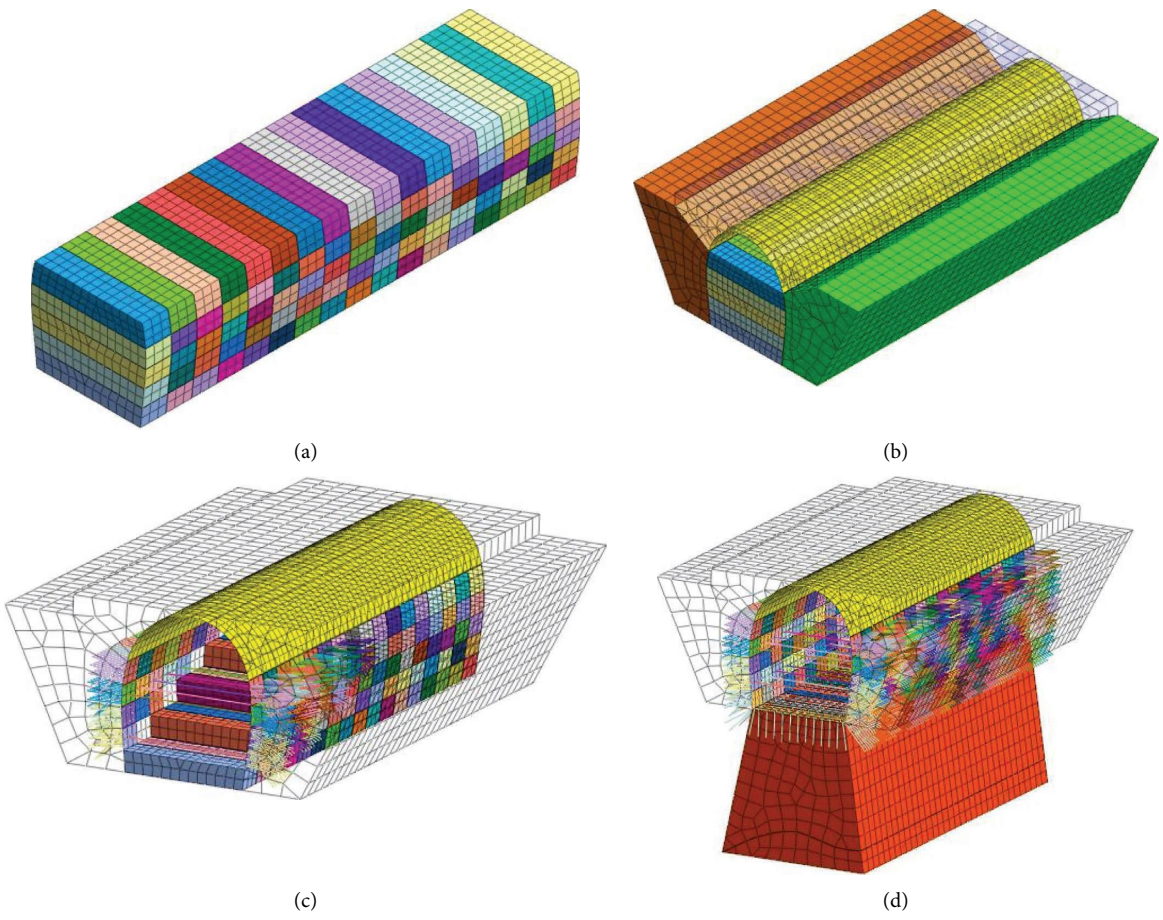

Figure 5: Key construction stages. (a) S1. (b) S3. (c) S11. (d) S30.

when it is not excavated to the target section. When the target section is excavated, the convergence rate increases rapidly. After the bottom grouting reinforcement, the slow and stable deformation stage shall be restored. (2) Concrete in the arch and grouting reinforcement on both sides are effective in controlling the rapid growth of horizontal convergence caused by the excavation of the entire first stage of an oversized section of the tunnel. (3) The growth rate of horizontal convergence in the excavation stage of the tunnel gradually decreases with the application of horizontal support, indicating that horizontal support is effective in controlling the large rate of horizontal convergence caused

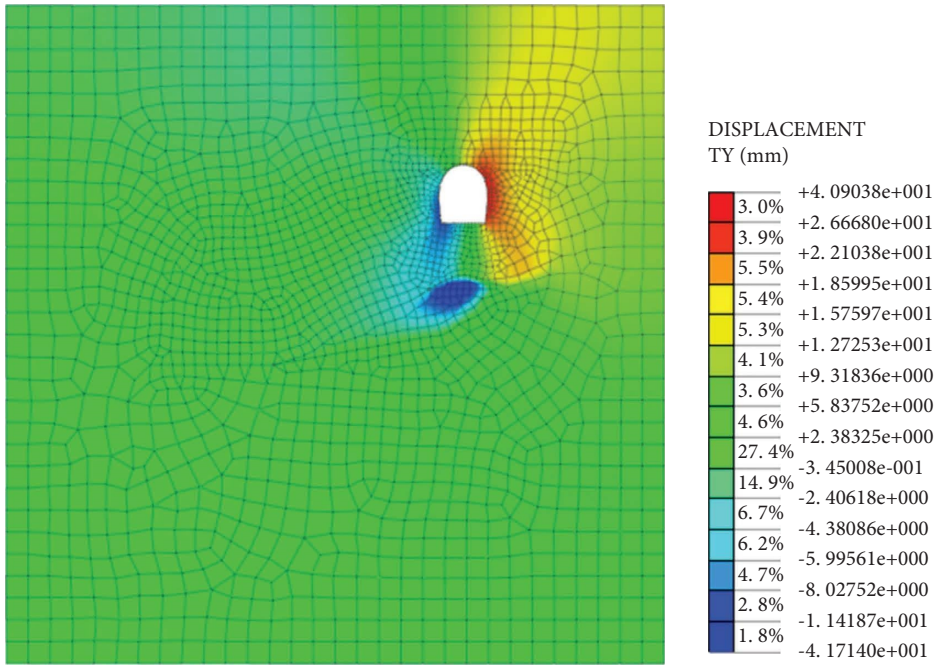

Figure 6: Cumulative total vertical displacement.

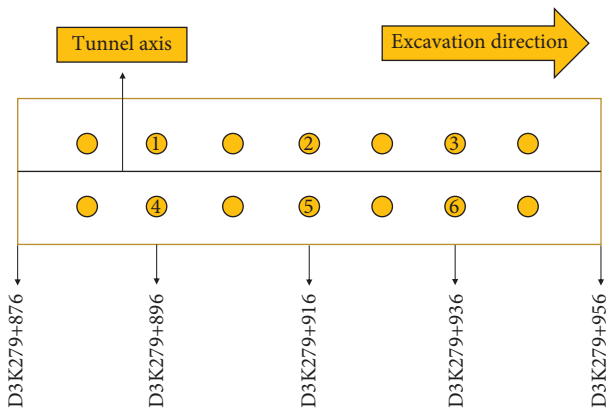

Figure 7: Schematic diagram of the arch waist taking point plan.

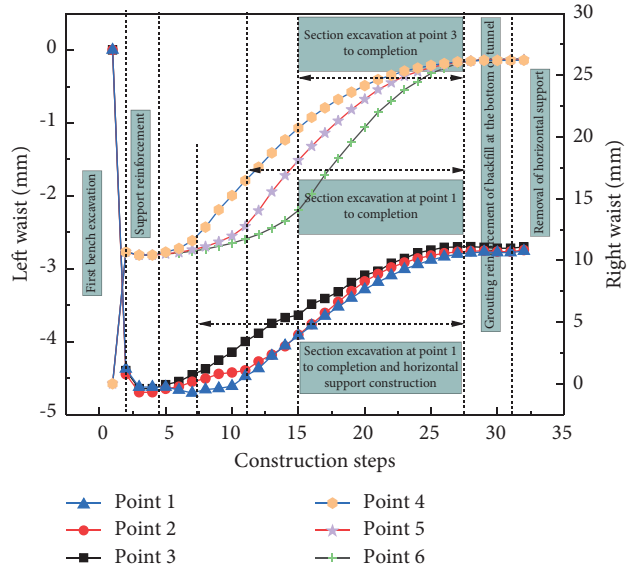

Figure 8: Displacement curves of the left and right arch waist.

by the excavation. (4) The maximum horizontal convergence of the first stage before the construction stage of section S14 at 916 is about 6.2 mm, the maximum accumulated horizontal convergence of the fourth stage after the completion of construction is about 19.7 mm, followed by about 19.5 mm for the third stage. Therefore, more attention should be paid to the monitoring and control of the horizontal convergence at the first stage in the early stage, and more attention should be paid to the monitoring and control of the horizontal convergence at the third and fourth stages in the later stage.

4.2. Stress Analysis. The maximum principal stresses in the initial stress state of the model and in the stable state after construction are shown in Figure 10. The positive values of the maximum principal stresses indicate tensile stresses and the negative values indicate compressive stresses. It can be seen that (1) under the influence of the giant cavern, the initial stress state of the model appears to have a complex distribution different from the usual uniform layered distribution of the geotechnical body. The larger values of the maximum principal stresses are mainly distributed in a "V" shape with the tunnel as the inflection point, showing a tensile stress state. Stress concentration occurs at the soft clay on the right side of the tunnel axis and near the two corners of the upper part of the model. The maximum principal stress of the surrounding rock on the right side of the tunnel is about 1.2 MPa, and the maximum principal stress of the soft clay is about 3.2 MPa, which is the

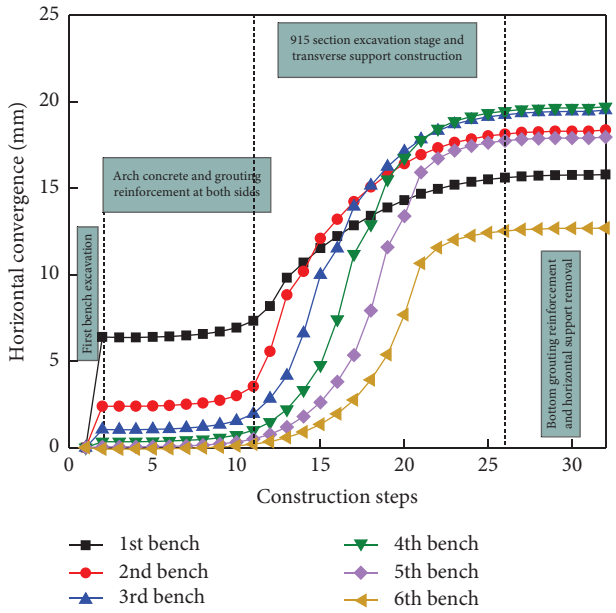

Figure 9: Horizontal convergence of each step at 916 section.

maximum value of the maximum principal stress in the tensile stress state of the whole model. (2) Under the influence of oversized tunnel excavation, the maximum principal stresses in the surrounding rock were redistributed after the construction was completed and stabilized. The concentration of stress occurs near the left waist and the right wall foot of the tunnel, which is in a state of tensile stress. The right waist and the left side wall footing of the tunnel are under compressive stress. Under the tensile stress state of the whole model, the maximum value of the maximum principal stress changes from the original soft clay to 5.3 MPa at the bottom of the right wall of the tunnel. The maximum principal stress in the tensile stress state at the left arch waist is 3.8 MPa, the maximum principal stress in the compressive stress state at the right arch waist is about 0.8 MPa, and the maximum principal stress in the compressive stress state at the foot of the left wall is 0.1 MPa. The overall distribution of the maximum principal stress of other rock and soil masses is basically unchanged, but the stress value decreases as a whole. The stress concentration from the larger value of the maximum principal stress is mainly transferred to the surrounding rock around the tunnel.

The minimum principal stresses in the initial stress state of the model and the stable state after construction are shown in Figure 11. It can be seen that (1) under the influence of the uneven distribution of rock and soil in the huge cavern, the minimum principal stress at the bottom of the model is in the state of compressive stress. In the lower left corner of the model, the small angle corner below the cavern, and the right edge of the cavern, there is a concentration of the minimum principal stress, with the maximum values of 14 MPa, 26 MPa, and 11 MPa, respectively. The minimum principal stresses in the surrounding rocks of the tunnel are all in the compressive stress state, with the right-hand side of the surrounding rocks being larger than the left-hand side, with a maximum value of around 2.7 MPa. (2) Under the influence of oversized section tunnel excavation, only the minimum principal stress distribution in the surrounding rock around the tunnel changed significantly after construction was completed and stabilized. The minimum principal stress near the left side arch waist and the right wall foot of the tunnel is concentrated, showing a state of tensile stress. The stress concentration near the right arch waist and the left wall foot of the tunnel is in a state of compressive stress. The maximum value of the minimum principal stress at the right wall foot of the tunnel is 0.1 MPa, and the maximum value of the minimum principal stress at the left arch waist is about 0.2 MPa. The maximum value of the minimum principal stress of the right arch waist is about 7.3 MPa, and the maximum value of the maximum principal stress of the left wall footing is about 4.8 MPa.

From the above analysis, the principal stress values of the surrounding rock around the tunnel after the model is stable are shown in Table 3. "+" indicates that the principal stress is tensile stress, and "−" indicates that the principal stress is compressive stress. It can be seen from the table that the value of one principal stress at one place of the surrounding rock is always very small or even close to zero relative to the other principal stress. Therefore, the maximum principal stress can be used to express the tensile stress state of the surrounding rock around the tunnel, and the minimum principal stress can be used to express its compressive stress state.

In order to further analyze the variation law of the principal stress of surrounding rock with the tunnel construction, extract the principal stress at the left arch waist, right arch waist, left wall foot, and right wall foot, and draw a temporal curve (see Figure 12). It can be seen from the figure that (1) during the whole construction process, the stress value at the right arch waist and wall foot is basically greater than that at the left arch waist and wall foot. This phenomenon is caused by the irregular shape of the giant karst cave and the complex distribution of rock and soil in it. The principal stress values at the left arch waist and the right wall foot are in tensile stress throughout the process, and the stress values at the left wall foot and the right arch waist are in compressive stress throughout the process. (2) With the construction of the tunnel, the principal stress values at the arch waist and the bottom of the wall increase as a whole. Due to the overall excavation of the first step of the cross-section tunnel, the principal stress at the arch waist increases rapidly. After the first step of anchor concrete support, arch concrete, and grouting reinforcement on both sides are completed, the principal stress value basically tends to be stable. After the excavation of the fifth step, the principal stress at the foot of the tunnel wall increases significantly. With the excavation and support, the principal stress decreases gradually and finally tends to be stable.

4.3. Horizontal Support Axial Force. Two layers of horizontal supports are set at the third step and the fifth step of the project. The distribution of the final axial force of the two

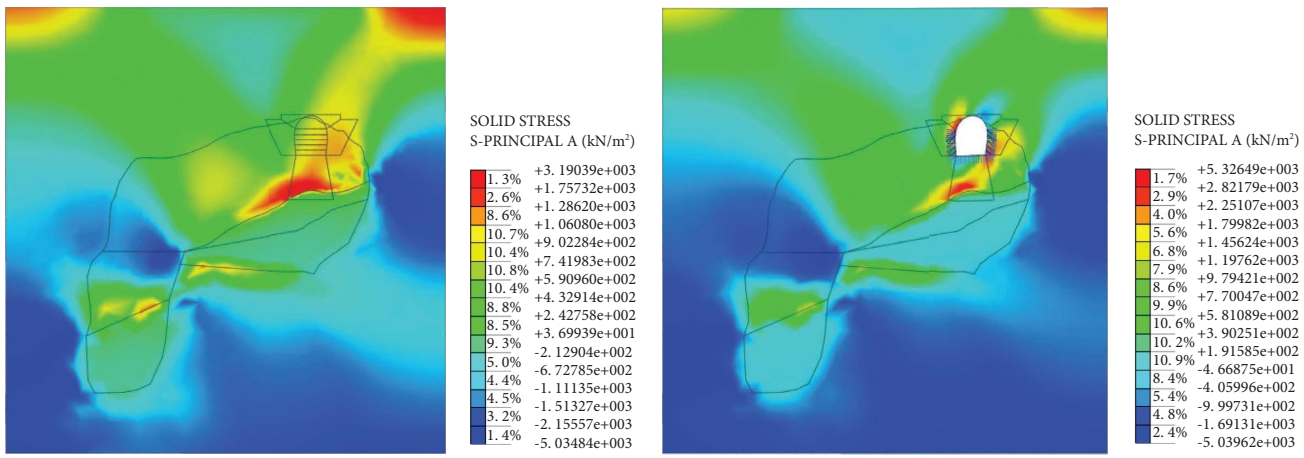

(a) (b)

Figure 10: Maximum principal stress distribution. (a) Initial stress state. (b) Stress state after model stabilization.

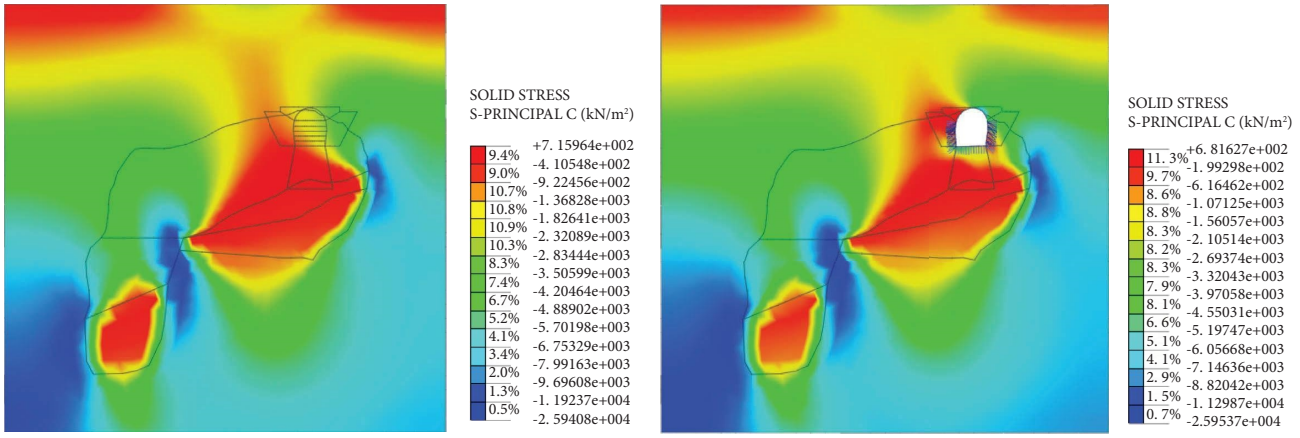

(a) (b)

Figure 11: Minimum principal stress distribution. (a) Initial stress state. (b) Stress state after model stabilization.

Table 3: Principal stress of surrounding rock after model stabilization.

Location	Maximum principal stress (MPa)	Minimum principal stress (MPa)
Left waist	+3.8	+0.2
Right waist	−0.8	−7.3
Left wall foot	−0.1	−4.8
Right wall foot	+5.3	+0.1

layers of horizontal supports on each excavation section is shown in Figure 13. It can be seen from the figure that the axial force distribution law of each cross-section of the two-layer cross support is basically the same, showing a pattern of "first decreasing, maintaining stability, and then decreasing." The axial force at the tunnel entrance is the largest, 270 kN for the first layer and 216 kN for the second layer. The axial force at the tunnel exit is the smallest, 148 kN for the first layer and 75.8 kN for the second layer. The axial force of the middle section decreases gradually with the increase in

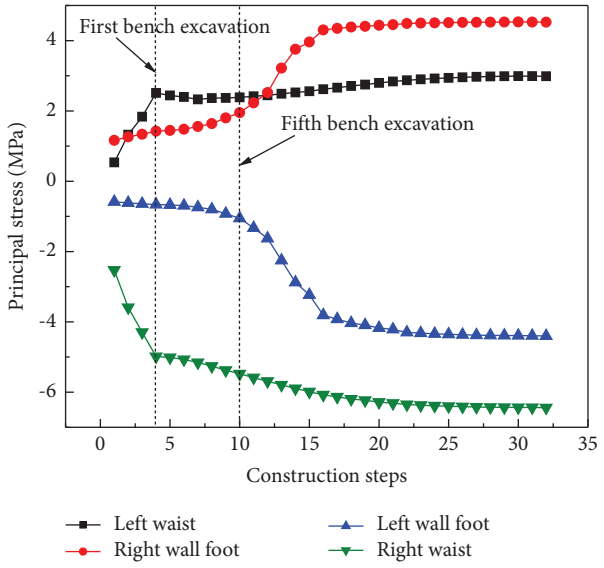

Figure 12: Temporal plot of principal stress values.

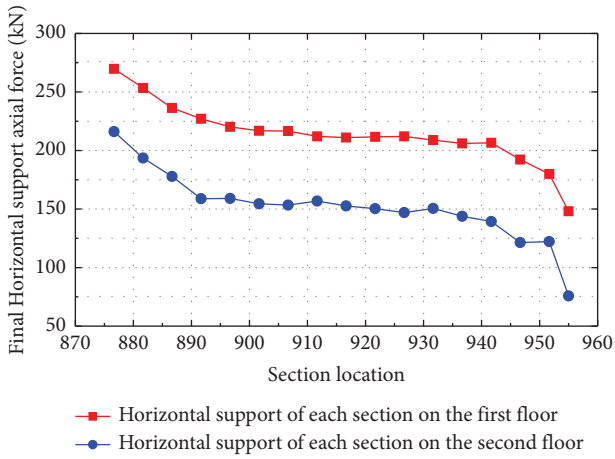

Figure 13: Distribution of final axial forces in two layers of horizontal supports at different sections.

excavation depth. Among them, the axial force of the 890–940 cross-section is basically the same. The first layer is about 210 kN, and the second layer is about 150 kN. The axial force of the first layer is generally greater than that of the second layer.

In the case of oversized cross-sectional tunnels through giant caverns, the law of change of the cross supports during the construction process should not be ignored either. Take the horizontal support at the section with the maximum axial force of the first and second floors as the research object, and draw the variation law of the axial force with the construction process, as shown in Figure 14. It can be seen that the variation law of the maximum axial force of the first-floor horizontal support and the second-floor horizontal support with the construction is basically the same. Firstly, the axial force increases rapidly when the horizontal support is just constructed. With the excavation of the corresponding bench to the completion of the excavation, the axial force value shows a trend where the growth rate gradually decreases and then tends to stabilize to reach the maximum axial force. The maximum axial force of the first layer is 270 kN, and the maximum axial force of the second layer is 216 kN. The axial force of the horizontal support on the rigid construction increases rapidly, so more monitoring and prevention should be carried out.

4.4. Plastic Zone Analysis. The state of distribution of the plastic zone in the important construction stage of the tunnel is shown in Figure 15. The red area in the figure indicates that the rock and soil mass is in a plastic-bearing state. Although plastic deformation occurs, the strength of the rock and soil mass does not decrease. The blue area indicates that the rock and soil mass are in a state of plastic loosening, and the strength decreases with plastic deformation. The green area indicates that the soil mass is in a tensile plastic failure state, and the colorless area indicates that the rock mass is in an elastic state.

(1) During the stage of the initial stress, some of the fragmented broken stone soil and almost all of the soft clay soils in the lower strength giant cavern fill are in a plastic-bearing state compared to the backfill and limestone. A few of the fragmentary broken stones are in the state of tensile plastic failure. The limestone at the lower right of the giant karst cave, where the broken stone soil contacts the block stone, is in a plastic-bearing state due to the shape of the small angle corner karst cave, which is prone to stress concentration. (2) In the S2 construction stage, due to the whole section excavation of the first step of the superlarge cross-section tunnel, although the corresponding bolting and concreting support was implemented in time, most of the rock mass in the plastic-bearing state in the initial stress state changed to plastic-loosening state. At the same time, both sides of the first step of the tunnel change from an elastic to plastic-bearing state. After the S3 stage arch crown concrete and grouting reinforcement on both sides, the rock and soil mass in the plastic-bearing state on the left side of the first step return to the elastic state, and the reinforcement effect is good. (3) After the excavation of the second bench in the S4 stage, the fill soil originally in the plastic-bearing area and the limestone at the small angle corner are all transformed into the plastic-loosening area. After the first layer of horizontal support is applied at the S7 stage and the second layer of horizontal support is applied at the S11 stage, part of the filling area is restored from the plastic-loose state to the plastic-bearing state. It shows that the construction of transverse bracing has a certain stable effect on the excavation process of the superlarge cross-section tunnel passing through a giant karst cave. (4) It can be seen from the state of the plastic zone from the S4 stage to the S11 stage that the plastic-bearing zone is mainly distributed at the right edge of the tunnel section during tunnel excavation, which is mainly caused by the asymmetry of rock and soil mass on both sides of the tunnel caused by the giant karst cave. In addition, the plastic-bearing area gradually develops downward with the continuous excavation of the steps. Therefore, during the excavation of the tunnel, the surrounding rock state at the right waist, foot, wall, and wall foot of the tunnel should be monitored and prevented. (5) All the tunnels were excavated in the S29 stage, and the plastic zone in the filling area deteriorated to a certain extent, but the plastic state improved after grouting reinforcement at the bottom of the tunnel in the S30 stage. After the removal of the horizontal support in the S31 stage, almost all the rock and soil mass in the original plastic-bearing state have changed to the plastic-loose state, but the tunnel as a whole is still in a stable state.

Therefore, although the state distribution of the plastic zone of the superlarge cross-section tunnel passing through the backfill of the giant cave is bad, it has been controlled to a certain extent after different reinforcement measures to ensure safe construction.

5. Site Monitoring

5.1. Site Monitoring Scheme. In situ, monitoring items include vault settlement and horizontal displacement, which are measured by a digital convergence meter, level gauge, and

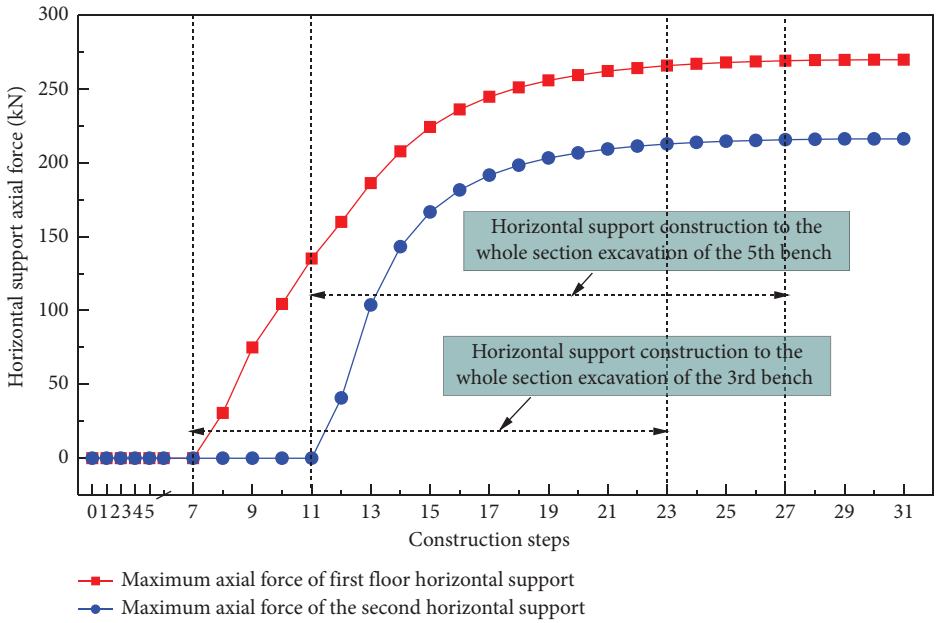

Figure 14: Maximum axial force horizontal support axial force.

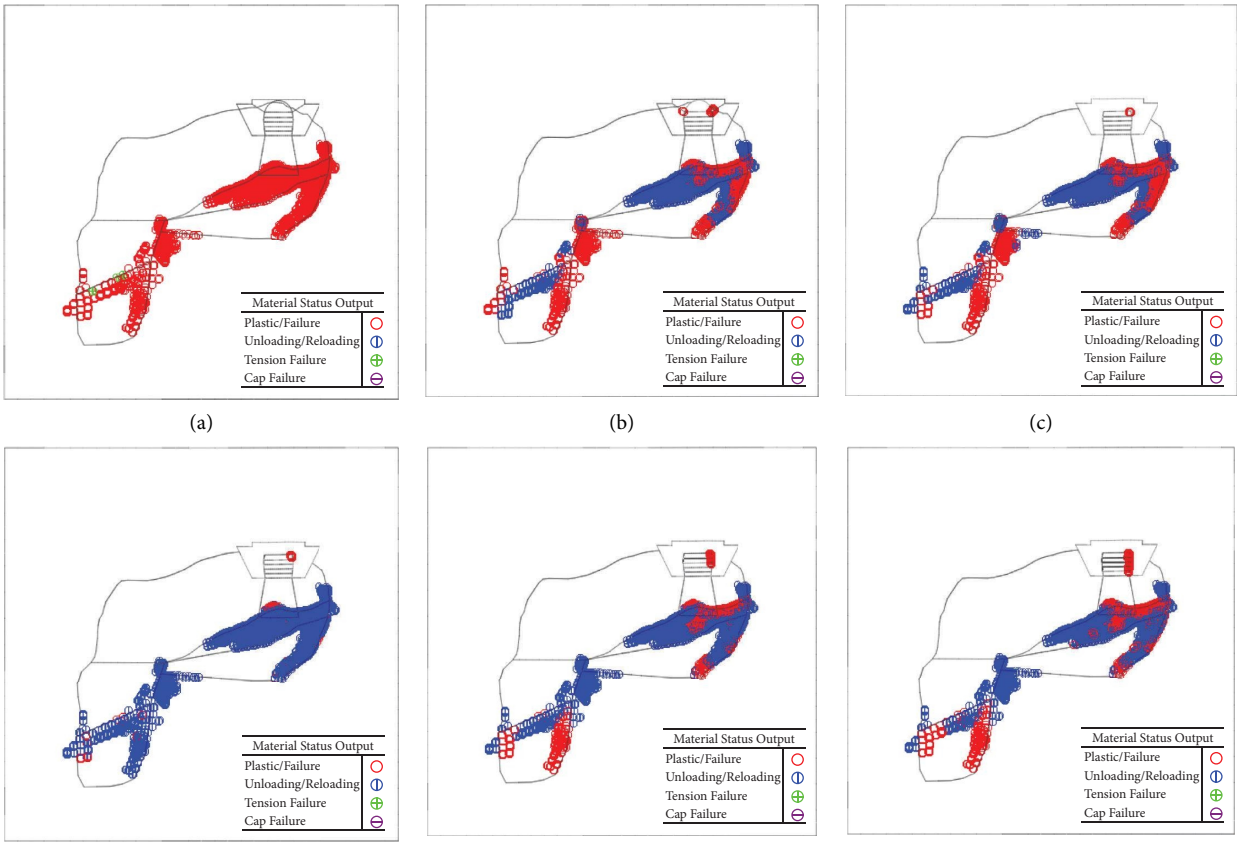

Figure 15: Continued.

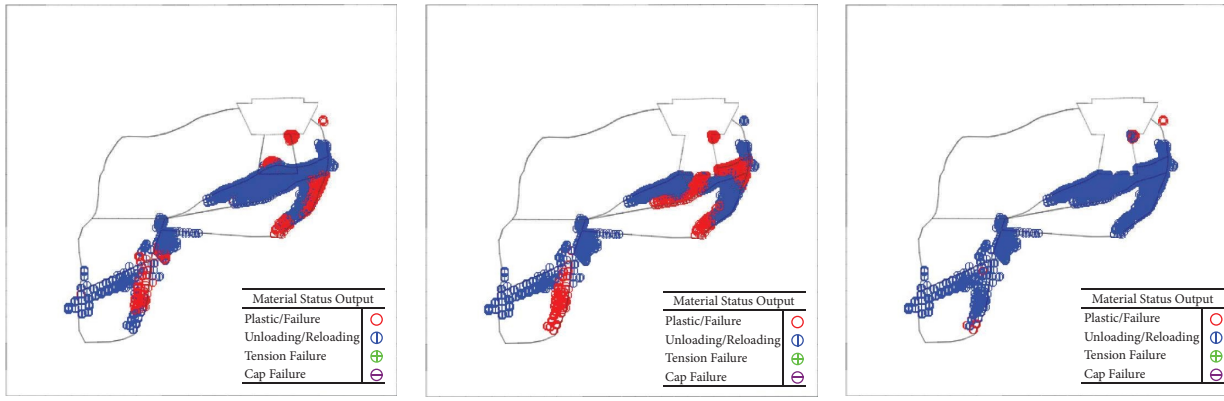

(g) (h) (i)

Figure 15: State of the plastic zone during the critical construction phase. (a) I.S. (b) S2. (c) S3. (d) S4. (e) S7. (f) S11. (g) S29. (h) S30. (i) S31.

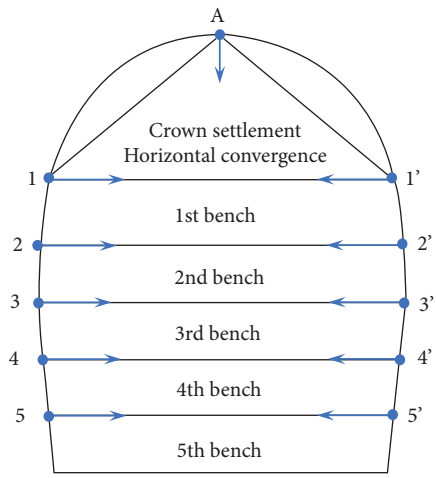

Figure 16: Monitoring scheme.

vibrating-wire receiver, respectively [58–61]. Through the above monitoring items, the changes in displacement could be obtained. Due to the limited space, this article only shows the displacement results of monitoring sections (the most critical section has been chosen) [36, 56, 57]. The specific section and its measuring point layout are shown in Figure 16.

5.2. Monitoring Data Analyses. The horizontal convergence monitoring data of section 916 during tunnel construction are presented in Figure 17.

It can be seen from the curve that (1) in the excavation and reinforcement stage of the first bench, the horizontal convergence value at the first bench is very small and basically remains unchanged. It shows that the anchor concrete support, vault concrete, and grouting reinforcement measures on both sides have a good control effect on the horizontal convergence caused by the overall excavation of the first bench. (2) From the second step of section D3K279 + 916 to the completion of bottom slab construction, the horizontal convergence value of each step increases rapidly. After backfilling the cavity behind the initial support, the growth of the horizontal convergence value of each step is restrained and tends to moderate. After the horizontal support is removed, the horizontal convergence value at the second step rebounds, but the horizontal convergence value at other steps does not increase. (3) During the whole construction process, the cumulative maximum value of horizontal convergence is about 17 mm, the numerical simulation result is about 19.7 mm, and the maximum error is 15.9%. The temporal variation law of horizontal convergence is slow growth in the early stage, rapid growth of deformation during excavation, and stable deformation in the later stage. This is basically consistent with the numerical simulation results.

The crown settlement monitoring data of sections 916~956 were selected for comparative analysis, as shown in Figure 18. The settlement curve of section D3K279 + 916~956 fluctuates in the range of 80 days. After grouting and backfilling, the final settlement is in a safe and stable range of between 0.4 mm and 13.5 mm. It took about three months for the accumulated crown settlement of the section to reach a stable state, and the final value was small.

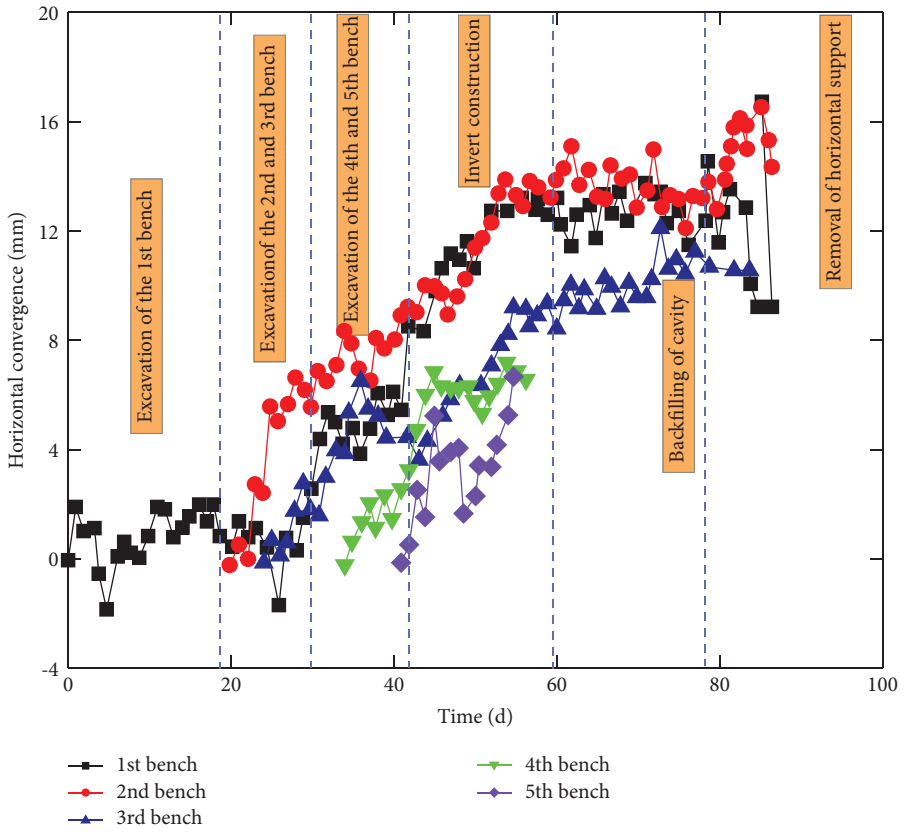

Figure 17: Horizontal convergence.

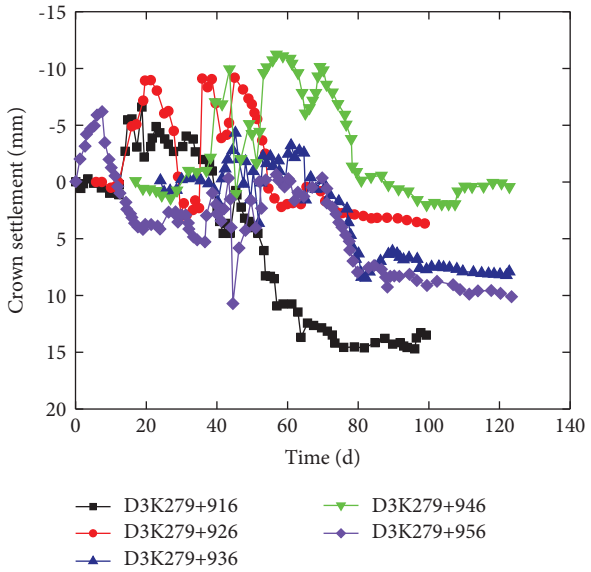

Figure 18: Crown settlement.

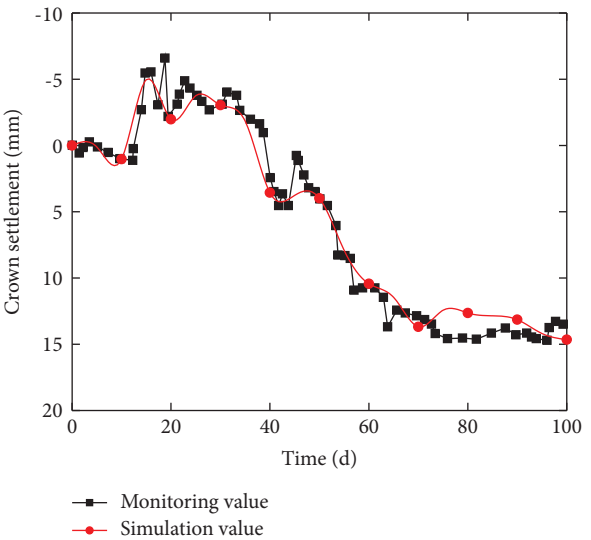

Figure 19: Comparison of simulation and monitoring data.

In order to further verify the accuracy of the numerical model, the crown settlement data for the key construction steps are extracted, as shown in Figure 19. The numerical calculation results are in good agreement with the settlement trend of the site monitoring data, and the final settlement error is 8.6%.

In summary, considering the complexity of the actual project at the site and the limitations of the simulation software, the results of the numerical simulation can be approximated as having high reliability.

6. Conclusions and Prospects

In this paper, the distribution characteristics and variation rules of the displacement stress field, horizontal support axial force, and plastic zone of surrounding rock and backfill body during the construction of a tunnel crossing a giant karst cave are analyzed. The main conclusions are as follows:

(1) During the excavation of the whole section of the first stage, the horizontal convergence and arch waist displacement values increased sharply. The deformation trend was effectively controlled after support and grouting, and the growth rate was reduced by 93%, and then remained stable.

(2) Under the initial stress state, the maximum principal stress is mainly distributed in a "V" shape with the tunnel as the inflection point, and the maximum value is 3.2 MPa in soft clay. The maximum value of the minimum principal stress is about 26 MPa at the small angle corner below the karst cave.

(3) The stress is redistributed after the model is stable. Stress concentration occurs in the area of the tunnel arch waist, and wall footing, which is easy to cause support damage. The maximum compressive stresses are 7.3 MPa and 4.8 MPa, and the maximum tensile stresses are 3.8 MPa and 5.3 MPa, respectively, which should be monitored more during the construction process. It is recommended to take antibuckling measures to strengthen local flexural rigidity and reduce the internal force and stress concentration. Also, the construction of bolts follows closely.

(4) The change law of the axial force of the two layers of horizontal support is basically the same, showing a sharp increase and a gradually stable growth trend. The axial force of the first layer of horizontal support is larger than that of the second layer, 270 kN and 216 kN, respectively, and the axial force is the largest at the entrance of the tunnel.

(5) The excavation disturbance of the tunnel leads to the deterioration of the rock and soil mass from the plastic-bearing state to the plastic-loose state. The reinforcement means such as grouting reinforcement and horizontal support will restore the rock and soil mass from the plastic-loose state to the plastic-bearing state. The plastic-bearing area is mainly distributed at the right edge of the tunnel section, and the plastic-bearing area gradually develops downward with the continuous excavation of the steps.

(6) The monitoring data show that the horizontal convergence and the crown settlement show a slow growth in the early stage and a rapid growth in deformation, and maintain a stable deformation trend. The numerical results are in good agreement with the site monitoring data. The average error of final settlement and peripheral convergence is 8.6% and 15.9%, respectively, which verifies the correctness of the numerical modeling method.

The above study is only a preliminary one on the mechanical behavior and convergence deformation law of surrounding rock and the horizontal support of the YJS tunnel through the giant cavern. The mechanical properties and internal force evolution law of the tunnel support structure can be explored subsequently, which verifies the feasibility of the tunnel design and construction plan. Meanwhile, model tests can be carried out on the settlement development of the backfill through indoor centrifugal tests to analyze the settlement development trend of the backfill and further verify the correctness of the numerical modeling method.

Data Availability

The data used to support the findings of this study are available from the corresponding author upon request.

Conflicts of Interest

The authors declare that they have no conflicts of interest.

Authors' Contributions

All authors have read and agreed to the published version of the manuscript.

Acknowledgments

This study was jointly supported by the National Nature Science Foundation of China (51908061), Project Program of Key Laboratory of Urban Underground Engineering of the Ministry of Education (grant no TUL2020-01), Construction Science and Technology Project of Xi'an (grant no. SZJJ2019-23), Key R&D Plan of Shaanxi Province (grant no. 2020SF-428), Fundamental Research Funds for the Central Universities, CHD (grant no. 300102212204), Project on Social Development of Shaanxi Provincial Science and Technology Department (grant no. 2021SF-474), and Key R&D Projects of China Railway Construction Kunlun Investment Group (grant no. KLTZ-KX01-2020-009).

References

[1] M. Garasic and D. Garasic, "Some new and interesting caverns in tunnels and along stretches of the Croatian Highways (Dinaric Karst, Croatia)," *Environmental Earth Sciences*, vol. 75, pp. 5–10, 2016.

[2] Q. Cui, H. Wu, S. Shen, Y. Xu, and G. Ye, "Chinese karst geology and measures to prevent geohazards during shield tunnelling in karst region with caves," *Natural Hazards*, vol. 77, no. 1, pp. 129–152, 2015.

[3] F. Niu, Y. Cai, H. Liao et al., "Unfavorable geology and mitigation measures for water inrush hazard during subsea tunnel construction: a global review," *Water*, vol. 14, no. 10, p. 1592, 2022.

[4] Z. Wang, Y. Cai, Y. Fang et al., "Local buckling characteristic of hollow π-type steel-concrete composite support in hilly-gully region of loess tunnel," *Engineering Failure Analysis*, vol. 143, Article ID 106828, 2023.

[5] Q. Fang, X. Liu, K. Zeng, X. Zhang, M. Zhou, and J. Du, "Centrifuge modelling of tunnelling below existing twin tunnels with different types of support," *Underground Space*, vol. 7, no. 6, pp. 1125–1138, 2022.

[6] X. Liu, W. Zhang, X. Gu, and Z. Ye, "Assessment of fatigue life for corroded prestressed concrete beams subjected to high-cycle fatigue loading," *Journal of Structural Engineering*, vol. 149, no. 2, Article ID 04022242, 2023.

[7] F. Han, J. Li, Y. Cai, Q. Wang, and J. Qiu, "Application of energy-concentrated hydraulic blasting technology in tunnel construction in China," *Shock and Vibration*, vol. 2022, Article ID 4724343, 17 pages, 2022.

[8] Y. Qin, J. Qiu, J. Lai et al., "Seepage characteristics in loess strata subjected to single point water supply," *Journal of Hydrology*, vol. 609, Article ID 127611, 2022.

[9] E. Ma, J. Lai, S. Xu, X. Shi, J. Zhang, and Y. Zhong, "Failure analysis and treatments of a loess tunnel being constructed in ground fissure area," *Engineering Failure Analysis*, vol. 134, Article ID 106034, 2022.

[10] Y. Xue, F. Kong, D. Qiu, M. Su, Y. Zhao, and K. Zhang, "The classifications of water and mud/rock inrush hazard: a review and update," *Bulletin of Engineering Geology and the Environment*, vol. 80, no. 3, pp. 1907–1925, 2021.

[11] Y. Xue, F. Kong, S. Li et al., "Water and mud inrush hazard in underground engineering: genesis, evolution and prevention," *Tunnelling and Underground Space Technology*, vol. 114, Article ID 103987, 2021.

[12] H. Fan, Y. Zhang, S. He, K. Wang, X. Wang, and H. Wang, "Hazards and treatment of karst tunneling in Qinling-Daba mountainous area: overview and lessons learnt from Yichang-Wanzhou railway system," *Environmental Earth Sciences*, vol. 77, no. 19, pp. 679–718, 2018.

[13] Y. Xue, P. G. Ranjith, Y. Chen, C. Cai, F. Gao, and X. Liu, "Nonlinear mechanical characteristics and damage constitutive model of coal under CO2 adsorption during geological sequestration," *Fuel*, vol. 331, Article ID 125690, 2023.

[14] Y. Xue, J. Liu, P. G. Ranjith, F. Gao, H. Xie, and J. Wang, "Changes in microstructure and mechanical properties of low-permeability coal induced by pulsating nitrogen fatigue fracturing tests," *Rock Mechanics and Rock Engineering*, vol. 55, no. 12, pp. 7469–7488, 2022.

[15] Z. Li, J. Lai, Z. Ren, Y. Shi, and X. Kong, "Failure mechanical behaviors and prevention methods of shaft lining in China," *Engineering Failure Analysis*, vol. 143, Article ID 106904, 2023.

[16] X. Weng, H. Li, J. Hu, L. Li, and L. Xu, "Behavior of saturated remolded loess subjected to coupled change of the magnitude and direction of principal stress," *International Journal of Geomechanics*, vol. 23, no. 1, Article ID 04022244, 2023.

[17] Y. Lv, Y. Jiang, W. Hu, M. Cao, and Y. Mao, "A review of the effects of tunnel excavation on the hydrology, ecology, and environment in karst areas: current status, challenges, and perspectives," *Journal of Hydrology*, vol. 586, Article ID 124891, 2020.

[18] X. Wang, J. Lai, S. He, R. Garnes, and Y. Zhang, "Karst geology and mitigation measures for hazards during metro system construction in Wuhan, China," *Natural Hazards*, vol. 103, no. 3, pp. 2905–2927, 2020.

[19] N. Zhang, Q. Zheng, K. Elbaz, and Y. Xu, "Water inrush hazards in the Chaoyang Tunnel, Guizhou, China: a preliminary investigation," *Water*, vol. 12, no. 4, p. 1083, 2020.

[20] X. Li, P. Zhang, Z. He, Z. Huang, M. Cheng, and L. Guo, "Identification of geological structure which induced heavy water and mud inrush in tunnel excavation: a case study on Lingjiao tunnel," *Tunnelling and Underground Space Technology*, vol. 69, pp. 203–208, 2017.

[21] G. Wu, W. Chen, J. Yuan, D. Yang, and H. Bian, "Formation mechanisms of water inrush and mud burst in a migmatite tunnel: a case study in China," *Journal of Mountain Science*, vol. 14, no. 1, pp. 188–195, 2017.

[22] J. Song, D. Chen, J. Wang et al., "Evolution pattern and matching mode of precursor information about water inrush in a karst tunnel," *Water*, vol. 13, no. 11, p. 1579, 2021.

[23] X. Li, Q. Zhang, X. Zhang, X. Lan, C. Duan, and J. Liu, "Detection and treatment of water inflow in karst tunnel: a case study in Daba tunnel," *Journal of Mountain Science*, vol. 15, no. 7, pp. 1585–1596, 2018.

[24] J. Qiu, F. Fan, C. Zhang, J. Lai, K. Wang, and F. Niu, "Response mechanism of metro tunnel structure under local collapse in loess strata," *Environmental Earth Sciences*, vol. 81, no. 5, p. 164, 2022.

[25] W. Shi, J. Qiu, C. Zhang et al., "Immersion mode and spatiotemporal distribution characteristic of water migration in loess tunnel," *Arabian Journal of Geosciences*, vol. 15, no. 7, p. 654, 2022.

[26] S. Xu, E. Ma, J. Lai et al., "Diseases failures characteristics and countermeasures of expressway tunnel of water-rich strata: a case study," *Engineering Failure Analysis*, vol. 134, Article ID 106056, 2022.

[27] X. Wang, F. Fan, and J. Lai, "Strength behavior of circular concrete-filled steel tube stub columns under axial compression: a review," *Construction and Building Materials*, vol. 322, Article ID 126144, 2022.

[28] S. He, J. Lai, Y. Li, K. Wang, L. Wang, and W. Zhang, "Pile group response induced by adjacent shield tunnelling in clay: scale model test and numerical simulation," *Tunnelling and Underground Space Technology*, vol. 120, Article ID 104039, 2022.

[29] Z. Li, J. Lai, Y. Li et al., "Ground fissure disasters and mitigation measures for hazards during metro system construction in Xi'an, China," *Arabian Journal of Geosciences*, vol. 15, pp. 5–16, 2022.

[30] W. Zhang, T. Lai, and Y. Li, "Risk Assessment of water supply network operation based on ANP-fuzzy comprehensive evaluation method," *Journal of Pipeline Systems Engineering and Practice*, vol. 13, no. 1, Article ID 04021068, 2022.

[31] W. Li, C. Zhang, D. Zhang, Z. Ye, and Z. Tan, "Face stability of shield tunnels considering a kinematically admissible velocity field of soil arching," *Journal of Rock Mechanics and Geotechnical Engineering*, vol. 14, no. 2, pp. 505–526, 2022.

[32] C. Liu, S. Zhou, C. Yu et al., "Damage behaviours of new-to-old concrete interfaces and a damage prediction model of reinforced concrete," *European Journal of Environmental and Civil Engineering*, vol. 26, no. 14, pp. 7138–7154, Article ID 1981459, 2022.

[33] H. Chen and C. Sha, "Stability analysis of surrounding rock and treatment structures in superlarge karst cave of naqiu tunnel," *Advances in Civil Engineering*, vol. 2018, Article ID 4842308, 14 pages, 2018.

[34] S. Li, J. Wu, Z. Xu, L. Zhou, and B. Zhang, "A possible prediction method to determine the top concealed karst cave based on displacement monitoring during tunnel construction," *Bulletin of Engineering Geology and the Environment*, vol. 78, no. 1, pp. 341–355, 2019.

[35] Z. Xu, P. Lin, H. Xing, D. Pan, and X. Huang, "Hydro-mechanical coupling response behaviors in tunnel subjected to a water-filled karst cave," *Rock Mechanics and Rock Engineering*, vol. 54, no. 8, pp. 3737–3756, 2021.

[36] Y. Zheng, S. He, Y. Yu, J. Zheng, Y. Zhu, and T. Liu, "Characteristics, challenges and countermeasures of giant karst cave: a case study of Yujingshan tunnel in high-speed railway," *Tunnelling and Underground Space Technology*, vol. 114, Article ID 103988, 2021.

[37] L. Zhang, H. Fu, J. Wu, X. Zhang, and D. Zhao, "Effects of karst cave shape on the stability and minimum safety thickness of tunnel surrounding rock," *International Journal of Geomechanics*, vol. 21, no. 9, Article ID 04021150, 2021.

[38] X. Zhou, H. Liu, C. Peng, and X. Wu, "Numerical simulation analysis of deformation effect on treatment structure of karst cave due to karst tunnel excavation," *Series on Rock and Soil Mechanics*, vol. 32, pp. 269–275, 2011.

[39] S. Li, D. Pan, Z. Xu et al., "A model test on catastrophic evolution process of water inrush of a concealed karst cave filled with confined water," *Series on Rock and Soil Mechanics*, vol. 39, pp. 3164–3173, 2018.

[40] Y. Xue, P. G. Ranjith, F. Gao, Z. Zhang, and S. Wang, "Experimental investigations on effects of gas pressure on mechanical behaviors and failure characteristic of coals," *Journal of Rock Mechanics and Geotechnical Engineering*, vol. 15, no. 2, pp. 412–428, 2023.

[41] L. Hou, X. Weng, J. Hu, and R. Zhou, "Undrained semi-analytical solution for cylindrical cavity expansion in anisotropic soils under biaxial stress conditions," *Journal of Rock Mechanics and Geotechnical Engineering*, vol. 15, no. 5, pp. 1284–1297, 2022.

[42] H. Fan, T. Liu, S. Zhang et al., "Effects of jet-grouting piles on loess tunnel foundation with centrifugal model tests," *International Journal of Geomechanics*, vol. 23, no. 3, Article ID 04022298, 2023.

[43] S. Xu, H. Nowamooz, J. Lai, and H. Liu, "Mechanism, influencing factors and research methods for soil desiccation cracking: a review," *European Journal of Environmental and Civil Engineering*, pp. 1–25, 2023, In Press.

[44] Y. Qin, J. Lai, G. Gao et al., "Failure analysis and countermeasures of a tunnel constructed in loose granular stratum by shallow tunnelling method," *Engineering Failure Analysis*, vol. 141, Article ID 106667, 2022.

[45] M. Mahmoudi, F. Boughalleb, S. Maaloul, M. Mabrouk, and R. Abdellaoui, "Phytochemical screening, antioxidant potential, and LC-ESI-MS profiling of ephedra alata and ephedra altissima seeds naturally growing in Tunisia," *Applied Biochemistry and Biotechnology*, pp. 1–13, 2023, In Press.

[46] T. Hua, S. Liu, X. Zhang, L. Meng, and P. Wang, "Numerical analysis of grouting of water-enriched karst highway tunnel based on critical water-enriched height," *Processes*, vol. 11, no. 1, p. 149, 2023.

[47] P. Peng, F. Peng, Z. Sun, and D. Zhang, "Grouting for tunnel stability control and inadequate grouting section recognition: a case study of countermeasure of giant karst cave," *Applied Sciences*, vol. 12, no. 23, Article ID 11895, 2022.

[48] Y. Xia, D. Xu, S. Qiu, X. Liu, X. Huang, and Z. Li, "Experimental study on mechanical properties of deeply buried granite during layered excavation of large underground caverns," *Rock Mechanics and Rock Engineering*, pp. 1–22, 2023, In Press.

[49] H. Fan, D. Zhou, Y. Liu et al., "Mechanical response characteristics of lining structure of pipeline karst tunnels in water-rich areas," *Rock and Soil Mechanics*, vol. 43, no. 7, pp. 1884–1898, 2022.

[50] C. Lin, C. Xia, H. Zhang, Z. Liu, and C. Zhou, "Simulated short-and long-term deformation in coastal karst caves," *Journal of Marine Science and Engineering*, vol. 10, no. 9, p. 1315, 2022.

[51] X. Wang, S. Wang, X. Peng, T. Ma, and B. Chen, "Equivalent numerical simulation method and application in karst-induced collapse of overlying sandy stratum," *Engineering Failure Analysis*, vol. 137, Article ID 106280, 2022.

[52] Y. Chen, C. Wang, M. Guo, and P. Lin, "Influence of concealed karst cave on surrounding rock stability and its treatment technology," *Journal of Shandong University*, vol. 50, pp. 33–43, 2020.

[53] Y. Li, S. Yang, J. Yu, and K. Gan, "Influence of a large karst cave on rock mass stability during tunnelling," *Model Tunnel Technology*, vol. 53, pp. 52–60, 2016.

[54] Y. Lin, *Study on Structure Selection Andoptimization Technology for Tunnel Crossing Large Karst Cave*, Chongqing Jiaotong University, Chongqing, China, 2018.

[55] K. Ye, *Study on the Compsive Treatment of Karst along the Tunnel of Chengdu-Guizhou Newly-Built Railway Line*, Southwest Jiaotong University, Chengdu, China, 2018.

[56] Y. Li, *Research on Construction and Settlement Control of Super-large Section High-Speed Railway Tunnel Passing through Giant Karst Cave*, Southwest Jiaotong University, Chengdu, China, 2021.

[57] X. Zhang, M. Carabello, T. Hill, K. He, C. R. Friese, and P. Mahajan, "Racial and ededchoac," *Frontiers in pediatrics*, vol. 7, pp. 525–531, 2019.

[58] Y. Xue, J. Liu, X. Liang et al., "Influence mechanism of brine-gas two-phase flow on sealing property of anisotropic caprock for hydrogen and carbon energy underground storage," *International Journal of Hydrogen Energy*, vol. 48, no. 30, pp. 11287–11302, 2022.

[59] Y. Qin, J. Lai, X. Cao, W. Zan, and Z. Feng, "Experimental study on the collapse evolution law of unlined tunnel in boulder-cobble mixed formation," *Tunnelling and Underground Space Technology*, vol. 10, 2022.

[60] Y. Qin, J. Lai, C. Li, F. Fan, and T. Liu, "Negative pressure testing standard for welded scar airtightness of waterproofing sheet for tunnels: experimental and numerical investigation," *Tunnelling and Underground Space Technology*, vol. 113, Article ID 104930, 2023.

[61] K. Wang, L. Yuhang, L. Zhonghao et al., "Rainfall deformation characteristics and influencing factors for a Large deep level landslide in tuff grounds in Zhejiang," *China Environmental Earth Sciences*, 2023.